

Chapter 6

RHESSI Observation of Chromospheric Evaporation: The 2003-11-13 M1.7 Flare¹

6.1 Introduction

Chromospheric evaporation was first suggested by Neupert (1968) to explain the origin of the hot, dense, soft X-ray-emitting plasma confined in the coronal loops during solar flares. The basic scenario is as follows. Magnetic reconnection leads to heating of the plasma and acceleration of particles high in the corona. The released energy is transported downward along the newly reconnected closed flaring loop by nonthermal particles and/or thermal conduction, heating the chromospheric material rapidly (at a rate faster than the radiative and conductive cooling rates) up to a temperature of $\sim 10^7$ K. The resulting overpressure drives a mass flow upward along the loop at a speed of a few hundred km s^{-1} , which fills the flaring loop with a hot plasma, giving rise to the gradual evolution of soft X-ray (SXR) emission. This process should also result in a derivative of the SXR light curve in its rising portion that closely matches the hard X-ray (HXR) light curve, which is called the Neupert effect and is observed in some (but not all) flares (Neupert, 1968; Hudson, 1991; Dennis & Zarro, 1993; Dennis et al., 2003; Veronig et al., 2005).

Hydrodynamic (HD) simulations of chromospheric evaporation have been carried out with an assumed energy transport mechanism (e.g., electron “beam” or conductive heating, Fisher et al., 1985c; Mariska et al., 1989; Gan et al., 1995; Yokoyama & Shibata, 2001; Allred et al., 2005) leading to various predictions on the UV-SXR spectral lines produced by the evaporated plasma, as well as the density and temperature profiles along the flaring loop. Most of the observational tests of these predictions rely on the blueshifted components of SXR emission lines produced by the up-flowing plasma, first reported by Doschek et al. (1980) and Feldman et al. (1980), who used spectra obtained from the *P78-1* spacecraft. Similar observations were subsequently obtained from X-ray spectrometers on the *Solar Maximum Mission* (*SMM*; Antonucci et al., 1982, 1984), the *Hinotori* spacecraft (Watanabe, 1990), the *Yohkoh* spacecraft (Wuelser et al., 1994), and the *Solar and Heliospheric*

¹Most of the material in this chapter was published in Liu, W., Liu, Jiang, & Petrosian (2006).

Observatory (*SOHO*; Brosius, 2003; Brosius & Phillips, 2004). Wuelser et al. (1994), on the other hand, observed co-spatial SXR blueshifts (upflows) and H α redshifts (downflows), as expected from HD simulations (Fisher et al., 1985a). A summary of relevant observations from *SMM* can be found in Antonucci et al. (1999).

All the aforementioned observations, however, were indirect evidence in the sense that the evaporation process was not imaged directly. On the basis of HD simulations, Peres & Reale (1993) derived the expected X-ray brightness profile across the evaporation front and suggested that the *Yohkoh* Soft X-Ray Telescope (SXT) or X-ray imagers with equivalent or better spatial and temporal resolution should be able to detect the front. Indeed, Silva et al. (1997) found that the HXR and SXR sources of the 1994 June 30 flare moved toward the loop top (LT) during the impulsive phase. Since the flare was located near the center of the solar disk, they identified such motions as the horizontal counterpart of the line-of-sight motion revealed by the blueshifted emission lines observed simultaneously by the *Yohkoh* Bragg Crystal Spectrometer (BCS).

RHESSI, with its superior spatial, temporal, and spectral resolution (Lin et al., 2002), provides us with opportunities to study the chromospheric evaporation process in unprecedented detail. We report in this chapter our analyses of the spatial and spectral evolution of a simple flare on 2003 November 13 with excellent *RHESSI* coverage. Because the flare occurred near the solar limb, it presented minimum projection effects and a well-defined loop geometry that allows direct imaging of the HXR brightness profile along the loop. The observations and data analyses are presented in §6.2, followed by a derivation of the evolution of the density profile along the flaring loop in §6.3. We summarize the major findings of this chapter and draw conclusions in §6.4.

6.2 Observations and Data Analyses

The flare under study is a *Geostationary Operational Environmental Satellite* (*GOES*) M1.7-class flare that occurred on 2003 November 13 in AR 0501 after it appeared on the east limb. This event followed a period of extremely high solar activities in late October and early November when a series of X-class flares, including the record-setting X28 flare of 2003 November 4, took place (Xu et al., 2004; Liu, W. et al., 2004a; Metcalf et al., 2005; Veronig et al., 2006). *RHESSI* had excellent coverage of this flare. Figure 6.1 shows the *RHESSI* and *GOES-10* light curves. The *GOES* 8-1 Å (1.6-12.4 keV) and 4.0-0.5 Å (3.1-24.8 keV) fluxes rise gradually and peak at 05:00:51 and 05:00:15 UT, respectively. The *RHESSI* high-energy (> 25 keV) count rates, on the other hand, exhibit two pulses peaking at 04:58:46 and 05:00:34 UT, the first one of which is stronger. The steps in the *RHESSI* light curves are due to the attenuator (shutter) movements (Lin et al., 2002). Before 04:57:57 UT and after 05:08:59 UT, there were no attenuators in, and between the two times the thin attenuator was in, except for a short period near 05:05 UT when the attenuator briefly moved out. Note that pulse pileup (Smith et al., 2002) has insignificant effects on this flare (see Appendix A.4.1 for details).

Figure 6.2 shows the evolution of the flare at different energies, which may be divided into three phases. (1) Before 04:57:57 UT is the rising phase, when the emission mainly comes from a flaring loop to the south. (2) Between 04:57:57 and 05:08:59 UT is the impulsive phase, during which another loop to the north dominates the emission. This loop appears to

share its southern footpoint (FP) with the loop to the south, which is barely visible because of its faintness as compared with the northern loop and *RHESSI*'s limited dynamic range of $\sim 10:1$. (3) After 05:08:59 UT is the decay phase, when the shutters are out and two off-limb sources (identified as the LTs of the two loops) dominate. The relatively higher altitudes compared with earlier LT positions are consequences of the preceding magnetic reconnection, as seen in several other *RHESSI* flares (Liu, W. et al., 2004a; Sui et al., 2004). Clearly the southern loop, which extends to a relatively higher altitude, evolves more slowly and is less energetic than the northern one. We focus on the evolution of the northern loop during the first HXR pulse (04:58-05:00 UT) in this chapter.

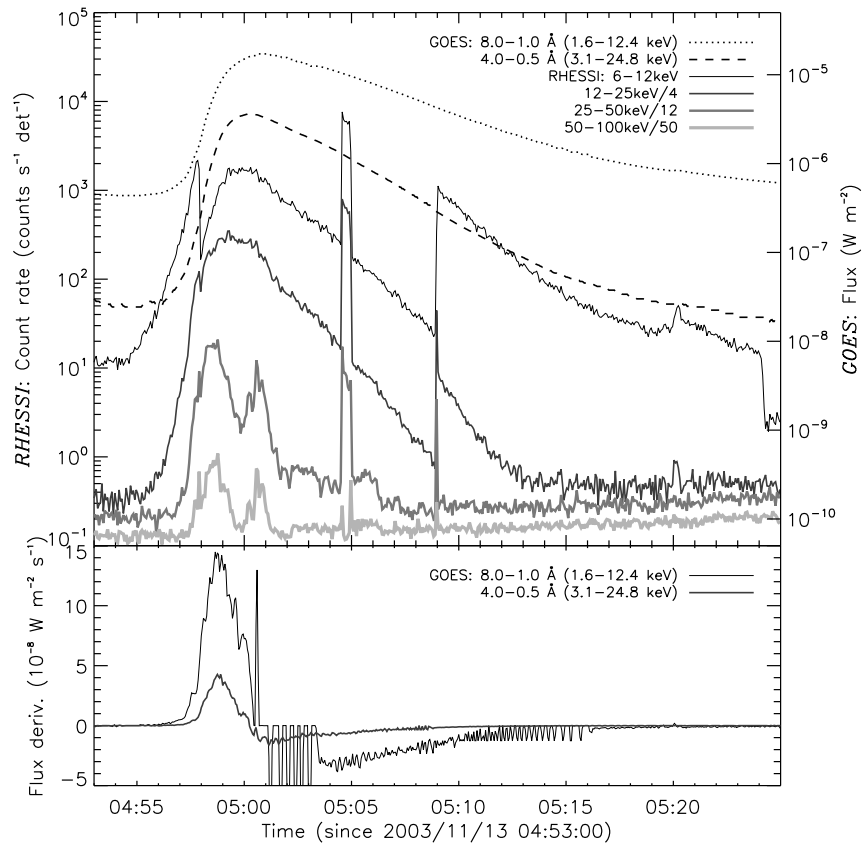


Figure 6.1: *Top*: *RHESSI* and *GOES-10* light curves. The *RHESSI* count rates are averaged over every 4 s, with scaling factors of 1, 1/4, 1/12, and 1/50 for the energy bands 6-12, 12-25, 25-50, and 50-100 keV, respectively. The sharp steps in the *RHESSI* light curves are due to attenuator state changes, and the sudden drop of the 6-12 keV count rate near 05:24 UT results from the spacecraft eclipse. The *GOES* fluxes in the bandpass of 8-1 Å (1.6-12.4 keV) and 4.0-0.5 Å (3.1-24.8 keV) are in a cadence of 3 s. *Bottom*: Time derivative of the *GOES* fluxes. Note that the periodic spikes of the low-energy channel after 05:00:24 UT are calibration artifacts [from Liu, W. et al. 2006].

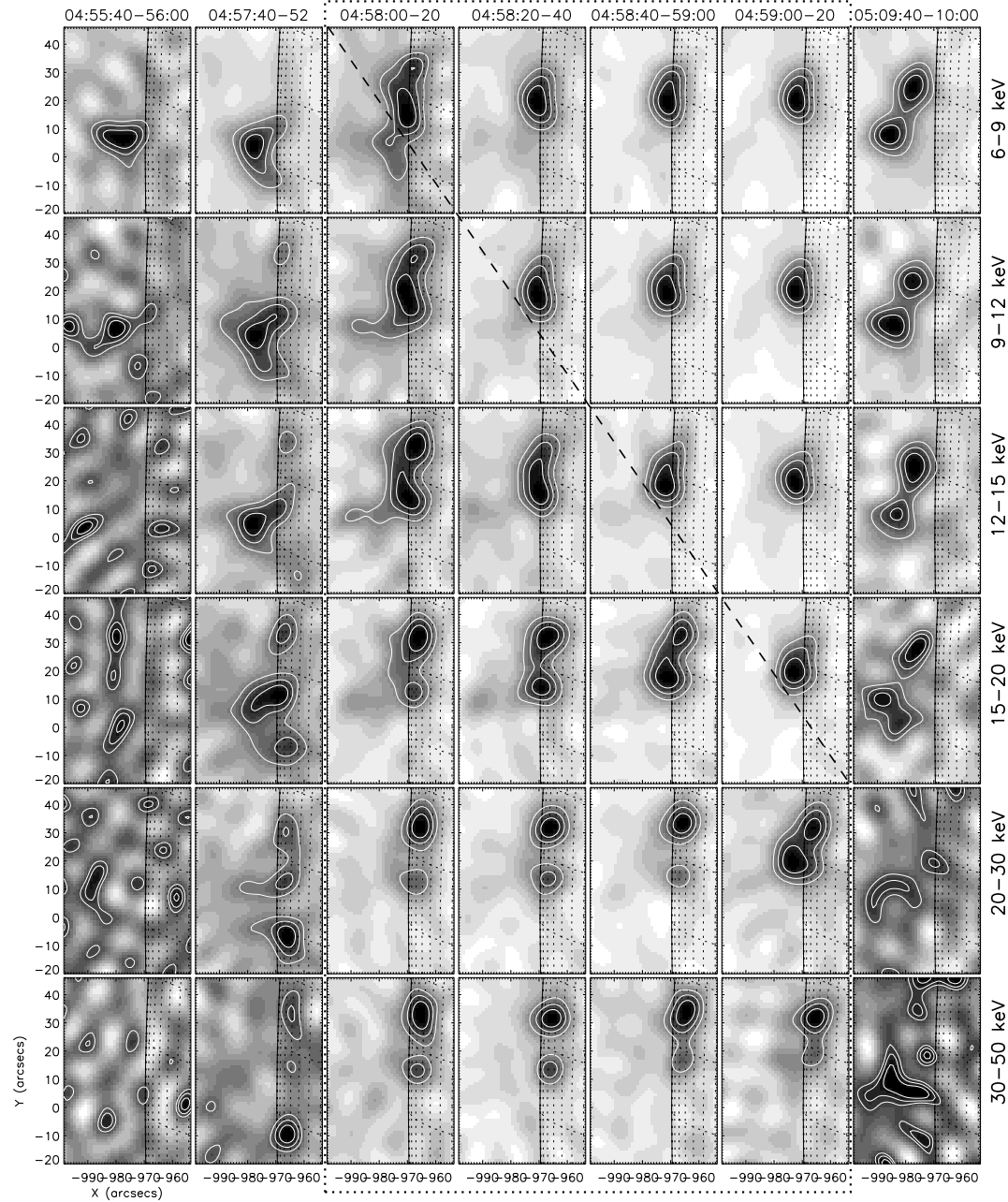


Figure 6.2: Mosaic of CLEAN images at different energies (*rows*) and times (*columns*). Contour levels are set at 40%, 60%, and 80% of the maximum brightness of each image. The front segments of detectors 3-6 and 8 were used for reconstructing these images and the others presented in this chapter, yielding a spatial resolution of $\sim 9.5''$. We selected the integration intervals to avoid the times when the attenuator state changed. The large dotted box encloses the images during the first pulse of the impulsive phase, and within this time interval the dashed diagonal line separates the frames showing double sources or an extended source from those with a compact single LT source [from Liu, W. et al. 2006].

6.2.1 Source Structure and Evolution

We now examine the images in greater detail. The top left panel of Figure 6.3 shows *RHESSI* CLEAN (Hurford et al., 2002) images of the northern loop at 9-12, 12-18, and 28-43 keV for 04:58:22-04:58:26 UT. (Although the 4 s integration time is rather short, the image quality is reliable, with a well-defined source structure.) At 9-12 keV the LT dominates and the emission extends towards the two FPs, which dominate the emission at 28-43 keV and above, with the northern FP (N-FP) much brighter than the southern one (S-FP). One of the most interesting features of the source structure is that emission from the legs of the loop dominates at the intermediate energy (12-18 keV). Similar structures are also observed for several other time intervals during the first HXR pulse (see discussions below). We find that emission from the legs is a transient phenomenon at intermediate energies, because when we integrate over a long period and/or a broad energy band, the LT and/or FP sources become dominant. To our knowledge, no images like this have been reported before. We attribute this in part to the relatively short integration time and to *RHESSI*'s high energy resolution.

For comparison with observations at other wavelengths, the same images at 9-12 and 28-43 keV (*solid contours*) are shown with the *SOHO* EUV Imaging Telescope (EIT), the Michelson Doppler Imager (MDI) magnetogram, and the MDI white-light maps in the other panels of Figure 6.3, where the dashed contours depict the southern loop at 6-9 keV for 04:57:40-04:57:52 UT. The EIT image at 04:59:01 UT (*top right*) shows emission at 195 Å that is co-spatial with the SXR emission from the northern loop. The brightest 195 Å emission, an indicator of the highest differential emission measure (and thus the highest density) at $\sim 1.3 \times 10^6$ K, appears to be close to the N-FP, which is also the strongest FP in HXRs.² The bottom left panel of Figure 6.3 displays the X-ray emission along with the post-flare (05:57 UT) MDI magnetogram. This clearly shows that the northern loop straddles a polarity reversal, with the brighter N-FP associated with a stronger magnetic field.³ The southern loop (*dashed contours*) is associated with an even weaker magnetic field. Here we show the MDI magnetogram recorded 1 hr after the flare's impulsive phase, because during a flare there are many uncertainties in the magnetic field measurement. The bottom right panel of Figure 6.3 shows the MDI continuum map at 12:47 UT (about 8 hr after the flare), suggesting that the flare occurred above the lower sunspot region (*dark area*). Note that during this interval the sunspot has moved westward about 4° in heliographic longitude. We do not plot the MDI white-light map at the time of the flare because then the sunspot was nearly on the limb and was barely visible.

Next we consider the evolution of the northern loop. We note that, as shown in the four columns for 04:58:00-04:59:20 UT (boxed by the dotted line) in Figure 6.2, the FPs

²EIT 195 Å passband images have a relatively narrow temperature response range, with a characteristic temperature of 1.3×10^6 K (see Dere et al., 2000, Fig. 12), and emission intensity would be lower for both higher and lower temperatures.

³Note that since this flare occurred near the solar limb, the line-of-sight magnetogram measures mainly the horizontal (parallel to the solar surface) component of the magnetic field. The vertical component is more relevant here because flaring loops are usually perpendicular to the surface. However, it would be reasonable to assume that the vertical component scales with the horizontal one, and the polarity reversal line in the latitudinal direction is essentially not subject to the line-of-sight projection effect, as seems very likely here.

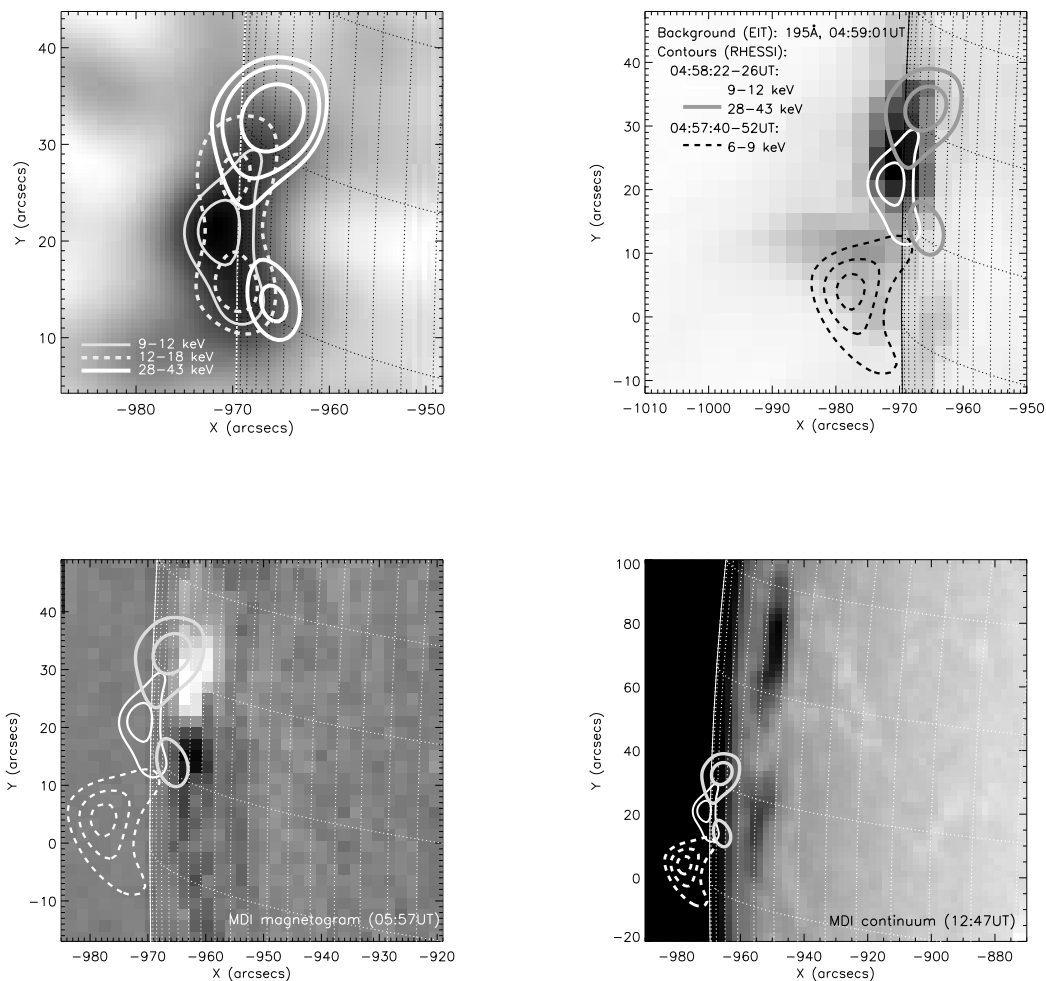


Figure 6.3: *Top left:* *RHESSI* images for 04:58:22-04:58:26 UT during the first HXR pulse. The background is the image at 9-12 keV. The contour levels are at 75 and 90% for 9-12 keV, 70% and 90% for 12-18 keV, and 50%, 60%, and 80% for 28-43 keV. *Top right:* EIT 195 Å image at 04:59:01 UT, showing co-spatial EUV emission in the northern HXR loop. The solid contours are the same as in the top left panel at 9-12 and 28-43 keV, except that the contour levels are 50% and 80% for the latter. A 6-9 keV *RHESSI* image (same as the second panel in the first row of Fig. 6.2) for 04:57:40-04:57:52 UT is plotted as dashed contours (at 50%, 70%, 90% levels) that depict the southern loop. The same set of contours is plotted in the two bottom panels as well. *Bottom left:* MDI magnetogram at 05:57 UT. The line-of-sight magnetic field in the map ranges from -351 G (*black*; away from the observer) to 455 G (*white*), with the FPs near the strong magnetic field regions. *Bottom right:* MDI continuum map at 12:47 UT, showing the sunspots. The heliographic grid spacing is 2° [from Liu, W. et al. 2006].

initially appear at all energies but later on dominate only in the high-energy bands, while the LT is first evident at low energies and becomes more and more prominent at relatively higher energies, as indicated by the dashed diagonal line. The emission from the LT also extends towards the legs at intermediate energies, and in a given energy band the emission concentrates more and more at the LT with time. These are expected to be common features of flares with a single loop because of chromospheric evaporation, which can increase the plasma density in the loop, making the LT dominant at progressively higher energies. However, because the 20 s integration time is relatively long, these images do not uncover the details of the evaporation process. To remedy this, we have carried out three different but complementary analyses of the images with higher time or energy resolution.

Temporal Morphological Evolution at Different Energies

To study the source morphology change over short time intervals, we model the loop geometry and study the evolution of the HXR brightness profile along the loop. We first

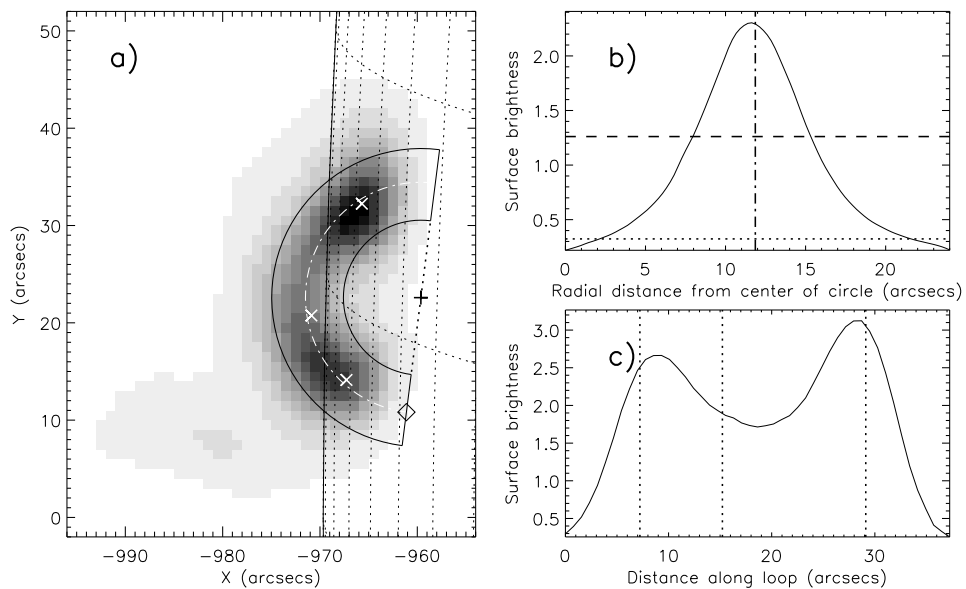


Figure 6.4: (a) Synthesized image obtained by superimposing 30 8 s images between 04:58:08 and 04:58:56 UT for 5 energy bands: 9–12, 12–15, 15–20, 20–30, and 30–50 keV. The three crosses mark one LT and two FP emission centroids of the corresponding sources in the 04:58:12–04:58:53 UT images at 6–9 and 50–100 keV, respectively. The solid lines represent the semi-circular model loop with the center of the circles, marked by the plus sign. The white dot-dashed line indicates the central arc (see below) of this loop, and the diamond indicates the start point of the distance in (c). (b) Radial brightness profile averaged along the loop, obtained from the image shown in (a). The distance is measured from the center of the circles. The horizontal dashed line marks the 50% level of the maximum, and the crossings of this line with the profile define the radii of the two solid semi-circles in (a). The 5% level is represented by the horizontal dotted line. The vertical dot-dashed line denotes the radial position of the central arc of the loop. (c) Same as (b), but for the surface brightness along the loop’s central arc, averaged perpendicular to the loop. The three vertical dotted lines mark the corresponding positions of the crosses in (a) [from Liu, W. et al. 2006].

made CLEAN images in two energy bands of 6-9⁴ and 50-100 keV over the time interval of 04:58:12-04:58:53 UT which covers the plateau portion of the first HXR pulse. From these two images we obtained the centroids (indicated by the white crosses in Fig. 6.4a) of the sources identified as the LT (6-9 keV) and the two FPs (50-100 keV), respectively. Assuming a semi-circular loop that connects the three centroids, we located the center of the circle, which is marked by the plus sign in Figure 6.4a. The gray scale in Figure 6.4a was obtained by superposition⁵ of 30 images (six 8 s intervals from 04:58:08 to 04:58:56 UT in five energy bands: 9-12, 12-15, 15-20, 20-30, and 30-50 keV) reconstructed with the PIXON algorithm (Metcalf et al., 1996; Hurford et al., 2002). Figures 6.4b and 6.4c, respectively, show the intensity profiles perpendicular to and along the loop (averaged over the respective orthogonal directions). The inner and outer circles (at $r = 8''.0$ and $15''.3$) in Figure 6.4a show the positions of the 50% values of the maximum intensity in Figure 6.4b. However, to infer the intensity profile along the loop, we use radially integrated flux down to the 5% level. This enables us to include as much source flux as possible (with little contamination from the southern loop). We define the mean of the radii at the 5% level as the radius of the central arc of the loop (indicated by the white dot-dashed line in Fig. 6.4a).

With the above procedure, one can study the evolution of the brightness profile along the loop at different energies. Figure 6.5 shows the results obtained from PIXON images with an integration time of one spacecraft spin period (~ 4 s) from 04:58:01 to 04:59:49 UT for three energy bands (20-30, 15-20, and 12-15 keV). Using a simple algorithm, we determine the local maxima whose slopes on both sides exceed some threshold value and mark them with filled circles. We compare each profile with its counterpart obtained from the CLEAN image (with the same imaging parameters) and use the rms of their difference to estimate the uncertainty as indicated by the error bar near the right-hand end of the corresponding profile. For each panel, the rms difference of all the profiles, as a measure of the overall uncertainty, is shown by the error bar in the upper right corner. This uncertainty is about 10% for the three energy bands; as expected, it increases slightly at higher energies, which have lower counts.

Figure 6.5a displays the profile at 20-30 keV, which, as expected (see Fig. 6.2), shows emission from the two FPs with fairly constant positions until the very last stage, when the LT emission becomes dominant.⁶ At this stage, the S-FP becomes undetectable and the

⁴Since the thin attenuator was in at that time, counts below 10 keV are likely dominated by photons whose real energy is about 10 keV higher than the detected energy. This is due to strong absorption of lower energy (< 10 keV) photons by the attenuator and escape of the germanium K-shell fluorescence photons that are produced by photoelectric absorption of higher energy (10-20 keV) photons in the germanium detector (see Smith et al., 2002, §5.2). However, for the flare under study, the 6-9 keV image most likely reveals the real LT morphology, because there are ample thermal photons at lower energies originating from the LT source and photons at slightly higher energies seem to come from the same location.

⁵Because we are interested in determining the average loop geometry during the first pulse when the low-energy X-ray flux has changed dramatically, using this approach to map the loop will ensure a relatively uniform brightness profile along the whole loop by assigning equal weights to images at different energies. On the other hand, if one simply integrates over the entire time range of 04:58:08-04:58:56 UT and the energy band of 9-50 keV, the source morphology will be dominated by the LT source that emits most of the photons at a later time and at relatively lower energies, which may not properly depict the loop geometry during the HXR pulse.

⁶As noted earlier, pulse pileup in the 20-40 keV range becomes relatively important at this late stage, meaning that a fraction of the 20-30 keV photons seen in the image are piled-up photons from lower energies.

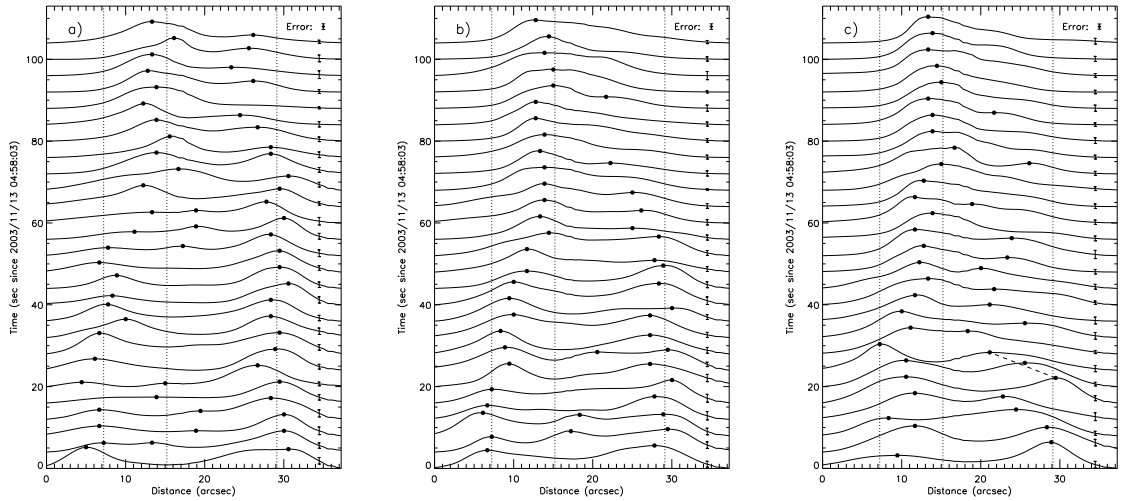


Figure 6.5: (a) Evolution of the 20-30 keV brightness profile along the loop in a cadence of 4 s starting at 04:58:03 UT. Each profile is normalized to its own maximum and has an integration time of 1 spacecraft spin period (~ 4 s) whose central time is used to label the vertical axis. The filled circles mark the local maxima, and the three vertical lines are the same as those in Fig. 6.4c. The error bar on each curve indicates an estimated uncertainty of the profile, and the stand-alone error bar in the upper right corner represents the overall uncertainty (13%) of all the profiles. (b, c) Same as (a) but for 15-20 and 12-15 keV, with an overall uncertainty of 12% and 10%, respectively. With the dashed straight line in (c), we estimate the speed of the emission maximum at $\sim 10^3$ km s $^{-1}$. Note the slightly different scales among the three panels for the profiles and their error bars [from Liu, W. et al. 2006].

N-FP has moved very close to the LT. At lower energies (15-20 keV; Fig. 6.5b) the maxima tend to drift toward the LT gradually and eventually merge into a single LT source. At even lower energies (12-15 keV; Fig. 6.5c) this trend becomes even more pronounced and the drift starts earlier, except that here the shift is not monotonic and there seems to be a lot of fluctuation. We also repeated the same analysis at a higher cadence (every 1 s, ~ 4 s integration interval) with both the PIXON and CLEAN algorithms. The evolution of the resulting profiles (although oversampled and thus not independent for neighboring profiles) appears to be in line with that shown here at a 4 s cadence obtained with PIXON. The general trends of these results indicate that high-energy HXR-producing electrons lose their energy and emit bremsstrahlung photons higher and higher up in the loop as the flare progresses. This can come about simply by a gradual increase of the density in the loop, presumably due to evaporation of chromospheric plasma. From the general drift of the maxima we obtain a timescale (\sim tens of seconds) and a velocity of a few hundred km s $^{-1}$, consistent with the sound speed or the speed of slow magnetosonic waves. As stated above, at low energies we see some deviations from the general trend, some of which do not appear to be random fluctuations. If so, and if we take one of the evident shorter timescale trends, that shown by the dashed line in Figure 6.5c, we obtain a large velocity⁷

⁷Among the highest observed upflow velocities in chromospheric evaporation are $\sim 10^3$ (Antonucci et al., 1990) and ~ 800 km s $^{-1}$ (Doschek et al., 1994), obtained from blueshifted Fe XXV spectra.

of 756 km s^{-1} that is comparable to the Alfvén or fast magnetosonic wave speed. This may indicate that another outcome of energy deposition by nonthermal particles is the excitation of such modes, which then propagate from the FPs to the LT and might be responsible for the circularly polarized zebra pattern observed in the radio band (Chernov et al., 2005). This, however, is highly speculative, because the spatial resolution ($\sim 7''$) is not sufficiently high for us to trust the shorter timescale variation. The longer timescale general trend, however, is a fairly robust result.

Energy-dependent Structure at Separate Times

Instead of examining the source structure with high time resolution, we can investigate it with higher energy resolution at longer integration intervals as a tradeoff for good count statistics and image quality. To this end, we have made PIXON images during three consecutive 24 s intervals starting from 04:58:00 in 20 energy bins within the 6-100 keV range. Figure 6.6 shows a sample of these images at 04:58:24-04:58:48 UT.

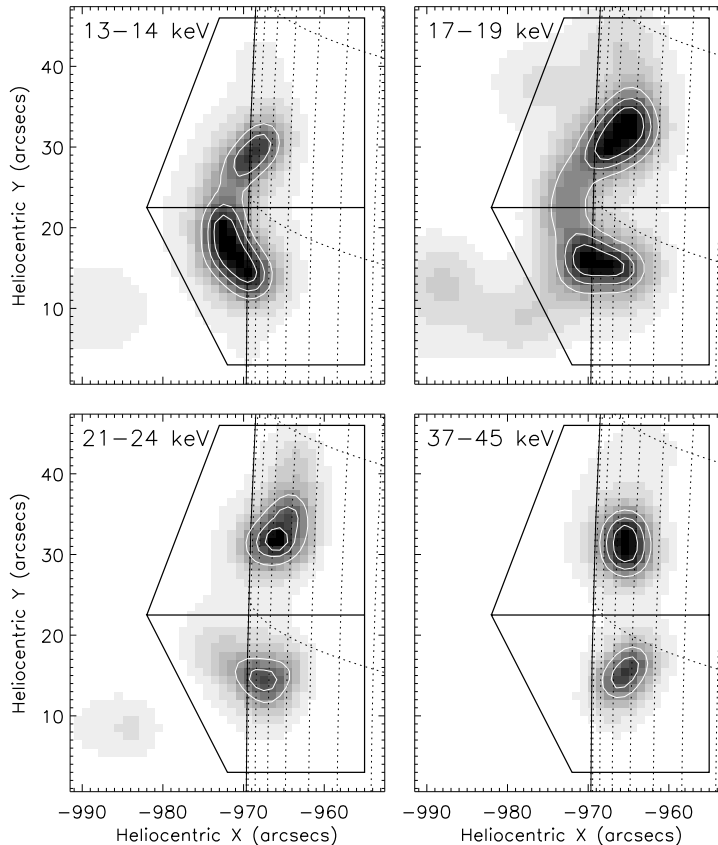


Figure 6.6: PIXON images at 04:58:24-04:58:48 UT in four energy bands. The overlaid polygons were used to divide the loop into halves to obtain the emission centroids [from Liu, W. et al. 2006].

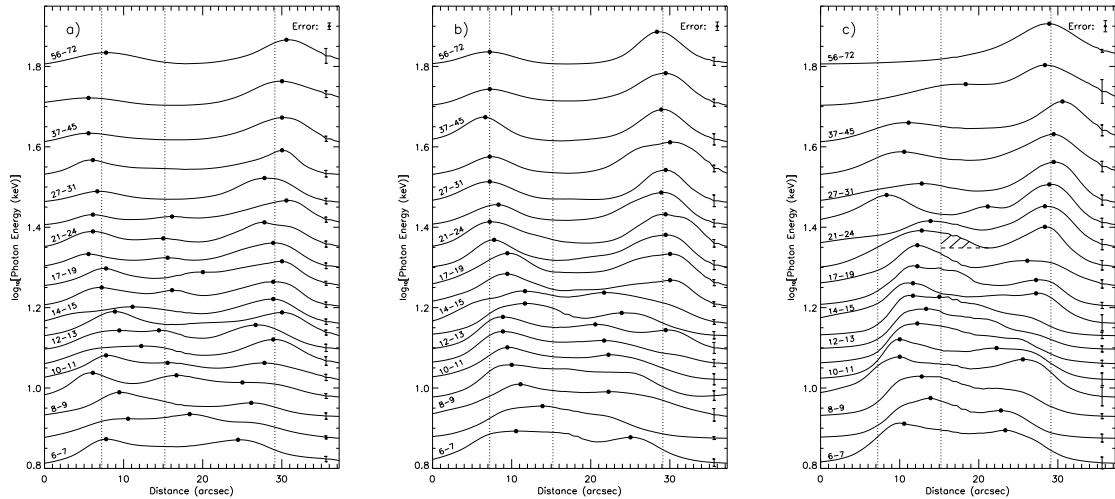


Figure 6.7: (a) Brightness profiles (obtained in the same way as in Fig. 6.5) at different energies for the time interval of 04:58:00-04:58:24 UT. The vertical axis indicates the average photon energy (in logarithmic scale) of the energy band for the profile. Representative energy bands (in units of keV) are labeled above the corresponding profiles. The vertical dotted lines are the same as in Figs. 6.4 and 6.5. (b, c) Same as (a) but for 04:58:24-04:58:48 and 04:58:48-04:59:12 UT, respectively. The error bars show the uncertainties of the corresponding profiles. The overall uncertainties, as indicated by the stand-alone error bar in the upper right corner of each panel (note different scales, similar to Fig. 6.5), are 14%, 13%, and 14%, respectively. The hatched region in (c) represents the LT emission (19-21 keV) removed for the derivation of the density distribution in Fig. 6.14 (see text) [from Liu, W. et al. 2006].

Figures 6.7a-6.7c show the X-ray emission profile along the loop at different energies for the three intervals.⁸ As in Figures 6.5a-6.5c, the high-energy emission is dominated by the FPs, but there is a decrease of the separation of the FPs with decreasing energies and with time. Again, at later stages the LT dominates and the profile becomes a single hump. The general trend again suggests an increase of the gas density in the loop. At lower energies (< 15 keV), the profile is more complicated, presumably due to many physical processes (in addition to chromospheric evaporation), such as thermal conduction and transport of high-energy particles, thermal and nonthermal bremsstrahlung, wave excitation and propagation, wave-particle coupling, and even particle acceleration, which may be involved. We believe that a unified treatment of acceleration and HD processes with physical conditions close to the flare is required for interpretation of these results to uncover the details.

To quantify this aspect of the source structure evolution, we divided the loop into two halves, as shown by the polygons in Figure 6.6, and calculated their emission centroids. The resulting centroids at the three times, together with the central arc of the model loop, are plotted in Figure 6.8. As can be seen, for each time interval the centroids are distributed along the loop, with those at higher energies being further away from the LT, and the entire pattern shifts toward the LT with time. Figure 6.9 shows the centroid positions of the northern half of the loop (where the source motions are more evident) along and

⁸Note that pileup effects, as discussed earlier, are insignificant during this period of time (see Fig. A.1).

perpendicular to the loop during the three intervals. This again shows that the higher energy emission is farther away from the LT and that the centroids shifted towards the LT with time, but similarly there are some complicated patterns at low and intermediate energies. All these are consistent with the general picture proposed above for the chromospheric evaporation process.

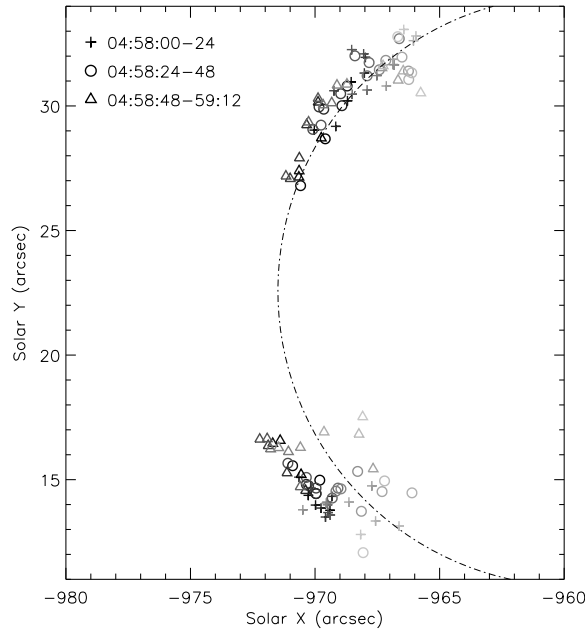


Figure 6.8: Centroids of the northern and southern halves of the loop at different energies for the three 24 s time intervals (same as those in Figs. 6.7a-6.7c). Energy increases from dark to light gray symbols. The dot-dashed line marks the central arc of the model loop (same as in Fig. 6.4a) [from Liu, W. et al. 2006].

Evolution of Overall Source Compactness

To further quantify the source motions, we obtained the brightness-weighted standard deviation or the second moment of the profiles. In general, the moment measures the compactness of the overall emission but does not yield the sizes of individual sources whose measurement is still challenging for *RHESSI* (Schmahl & Hurford, 2002). Hence, our attention should be paid to the general trend of the moment rather than to its absolute values, which may be subject to large uncertainties and thus may be less meaningful. The moments of the profiles resulting from CLEAN images (in three energy bands over 8 s intervals) are plotted in Figure 6.10b. There is a general decrease of the moment, with the decline starting earlier at lower energies. Such a decrease is expected if the two FPs move closer to each other. However, caution is required here because a decrease of this quantity could also come about by other causes, say, by an increasing dominance of the brightest source. We therefore checked the original images and the corresponding profiles when interpreting our results. To estimate the uncertainty of the moment, for each energy band we repeated the

calculation with different integration time (6.10c). The resulting moments remain essentially unchanged, and, as expected, the fluctuations of the moment decrease with increasing integration time. We also plot in 6.10c the moment (*solid curve*) obtained from PIXON images with an integration time interval of two spin periods (~ 8 s), which basically agrees with its CLEAN counterpart in the general trend. The gradual⁹ decrease of the moment is consistent with the motion of the centroids of sources up the legs of the loop, which can take place by a continuous increase of the gas density in the loop due to evaporation.

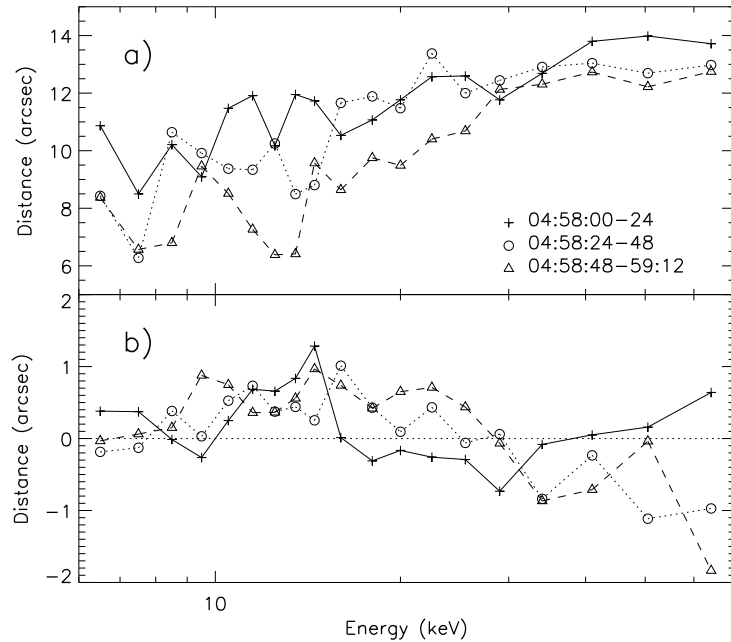


Figure 6.9: Positions of the northern centroids projected along (a) and perpendicular to (b; note the different scales) the central arc (the line in Fig. 6.8) of the loop. The distance in (a) is calculated from the average LT position, as shown in Fig. 6.4a [from Liu, W. et al. 2006].

6.2.2 Spectral Analysis

Spectral analysis can be used to study the evaporation process as well. With an isothermal plus power-law model, we fitted the spatially integrated *RHESSI* spectra down to 6 keV (Smith et al., 2002) for every 8 s interval during the impulsive phase. The emission measure (EM) and temperature of the isothermal component (*asterisks*) are plotted in Figures 6.10d and 6.10e, respectively. The EM rises almost monotonically with time from 0.6 to $14.2 \times 10^{49} \text{ cm}^{-3}$. This translates into an increase of the plasma density [$n = (\text{EM}/V)^{1/2}$] by a factor of ~ 5 if we assume a constant volume V . The temperature remains almost constant with a trend of slight decrease with time. The EM and temperature derived from the *GOES* data (*plus signs*) are also shown for comparison. In general, the *GOES* results are smoother and the temperature increases monotonically but remains below that of the *RHESSI* data,

⁹On the other hand, the jumps (if real) of the moment may suggest a transient phenomenon.

consistent with previous results (Holman et al., 2003). This is expected because *RHESSI* is more sensitive to higher temperatures than *GOES*. However, surprisingly, the *GOES* emission measure is also lower than that of *RHESSI*, as opposed to what is the case more generally (see Holman et al., 2003). It is not clear whether or not this is due to a problem related to the *RHESSI* calibration at low energies. Nevertheless, the continuous increase of the EM at comparable rates does suggest a gradual increase of the plasma density.

The best-fit parameters of the power-law component with a low-energy cutoff are plotted in Figure 6.10*f*. The power-law index γ (*plus signs*) is anti-correlated with the high-energy light curves (see Fig. 6.10*a*) and shows a soft-hard-soft behavior. It starts at 4.43 at 04:58:02 UT, drops to 3.82 at the impulsive peak (04:58:26 UT), and rises to 7.12 at 04:59:46 UT. The high indexes (> 5) may be an indicator of high-temperature thermal rather than nonthermal emission. Thus, in what follows we limit our analysis to times up to 04:59:20 UT. The low-energy cutoff (*asterisks*) of the power law is about 15 keV and is near the intersection of the isothermal (exponential) and power-law components.

6.2.3 The Neupert Effect

The Neupert effect is commonly quoted as a manifestation of chromospheric evaporation (Dennis & Zarro, 1993), and a simple energy argument (e.g., Li et al., 1993) is often used to account for the relationship between SXR and HXR fluxes (F_{SXR} and F_{HXR}). In the thick-target flare model, the nonthermal F_{HXR} represents the *instantaneous* energy deposition rate ($\dot{\mathcal{E}}_e$) by the electron beam precipitating to the chromosphere, but the thermal F_{SXR} is proportional to the *cumulative* energy deposited; that is, the time integral of $\dot{\mathcal{E}}_e$. It naturally follows that the temporal derivative of the SXR flux, \dot{F}_{SXR} , should be related to F_{HXR} .

The simplest test of the Neupert effect is usually carried out by plotting \dot{F}_{SXR} and F_{HXR} in some energy band. There are many reasons why a simple linear relationship would not be the case here. The first and most important is that $\dot{\mathcal{E}}_e$ is related to F_{HXR} through the bremsstrahlung yield function Y ($F_{HXR} = \dot{\mathcal{E}}_e Y$), which is not a constant and depends on the spectrum of the electrons or HXRs (see, e.g., Petrosian 1973). Here the most crucial factor is the low-energy cutoff (E_1) of the nonthermal electrons, but the spectral index also plays some role. The total yield of all the bremsstrahlung photons produced by a power-law spectrum of electrons with energies above E_1 (in units of 511 keV) is

$$Y_{total} = \frac{16}{3} \left(\frac{\alpha}{4\pi \ln \Lambda} \right) E_1 \left(\frac{\delta - 2}{\delta - 3} \right), \quad (6.1)$$

and the yield of the photons whose energies are greater than E_1 is

$$Y_{E_1} = \frac{16}{3} \left(\frac{\alpha}{4\pi \ln \Lambda} \right) E_1 \left(\frac{2}{\delta - 1} \right)^2 \left(\frac{1}{\delta - 3} \right), \quad (6.2)$$

where $\alpha = 1/137$, $\ln \Lambda = 20$ is the Coulomb logarithm, and δ is the spectral index of the power-law electron flux. We plot in Figure 6.11 Y_{E_1} as a function of δ for $E_1 = 20$ keV. As shown in Figure 6.10*f*, both the low-energy cutoff and the spectral index of the nonthermal emission vary during the pulse, indicating variations in the electron spectrum and thus breaking the linearity of the SXR-HXR relationship. Other factors that can also produce

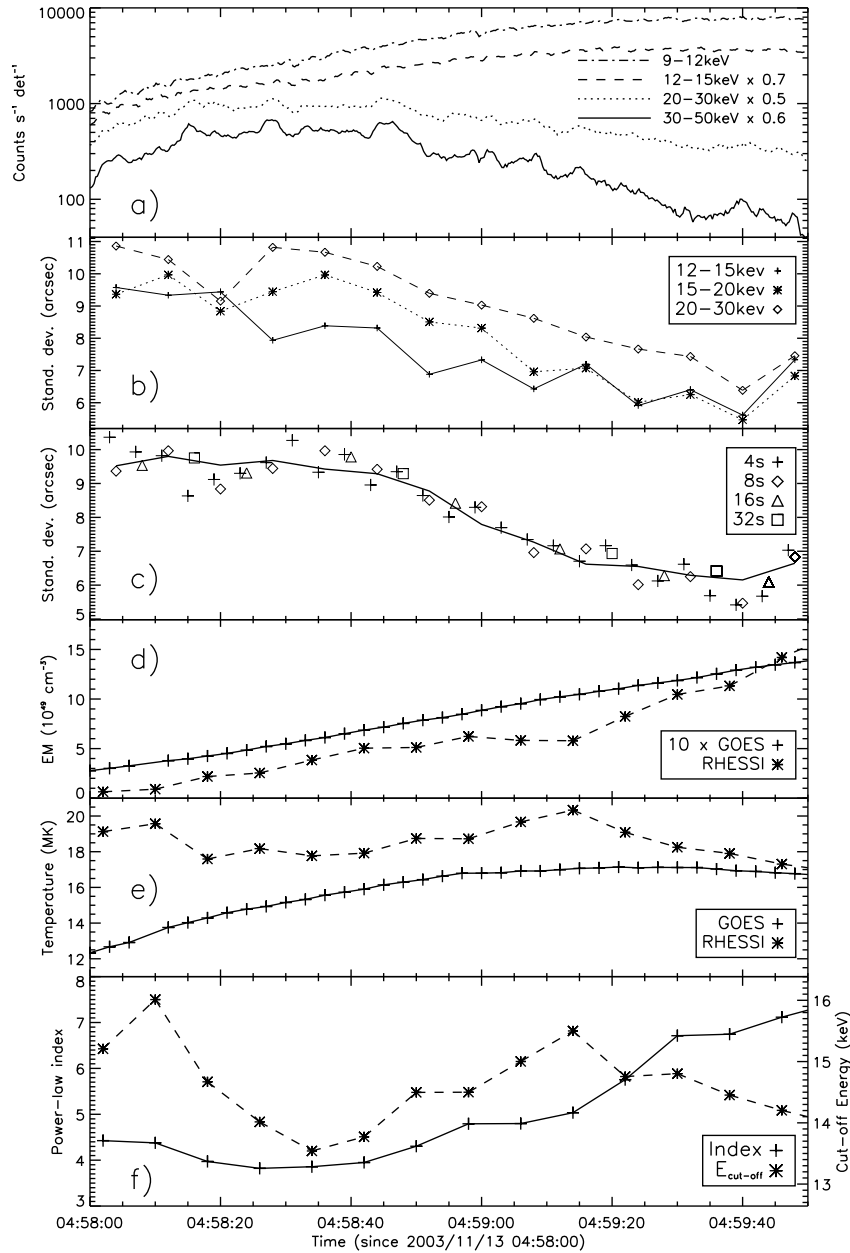


Figure 6.10: (a) *RHESSI* light curves (demodulated to remove artificial periodicity caused by the spacecraft spin). (b) Evolution of the standard deviation of the brightness profiles along the loop in three different energy bands obtained from CLEAN images. (c) Same as (b) but in the 15-20 keV band and with different integration time intervals indicated in the legend. The solid curve denotes the result from the PIXON images with an ~ 8 s integration time interval. (d, e) Evolution of the emission measure (in units of $10^{49} cm^{-3}$) and temperature (in units of MK), respectively, of the thermal component of the spatially integrated *RHESSI* spectrum obtained from fits to a thermal plus power-law model and from thermal fits to the *GOES* spectrum. The *GOES* emission measure is scaled by a factor of 10. (f) Evolution of the power-law index and the low-energy cutoff of the *RHESSI* power-law component [from Liu, W. et al. 2006].

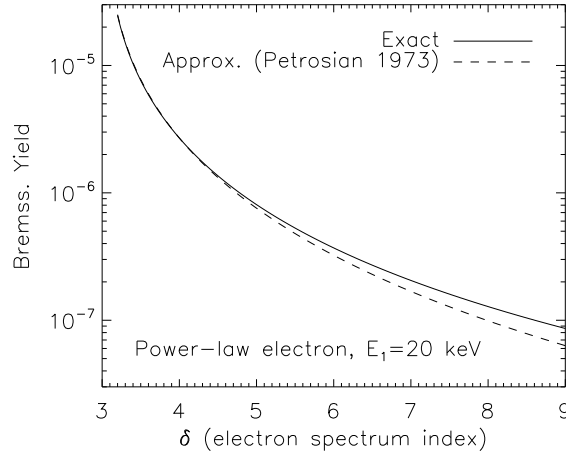


Figure 6.11: Bremsstrahlung yield in the thick-target model for a power-law electron spectrum with a low-energy cutoff of $E_1 = 20$ keV. The dashed line corresponds to the approximate result from eq. (6.2) here or eq. (30) in Petrosian (1973). The solid line comes from more accurate results from numerical integration of eq. (29) in Petrosian (1973).

further deviations are energy deposition by protons (and other ions), by conduction, and possible ways of dissipation of energy other than simply heating and evaporating the chromospheric plasma by nonthermal electrons. A detailed treatment of the problem requires solutions of the combined transport and HD equations, which is beyond the scope of this chapter. Veronig et al. (2005), who included some of these effects in an approximate way, found that the expected relationship was mostly not present in several *RHESSI* flares. Finally, one must include the fact that the chromospheric response of SXR emission will be delayed by tens of seconds, depending on the sound travel time (and its variation) and other factors.

The flare under study has shown no indication of gamma-ray line emission, which means that the contribution of protons most probably is small. In the currently most favorable model, in which the electrons are accelerated stochastically by turbulence (see, e.g., Petrosian & Liu, 2004) The turbulence can suppress heat conduction during the impulsive phase and possibly also during the decay phase (Jiang et al., 2006). Because there do not appear to be large changes in the shape of the loop during the impulsive phase, other energy dissipation processes, such as cooling by expansion, may also be negligible. Assuming these to be the case, we have performed the Neupert effect test in two ways, the first of which is the common practice of examining the relation between \dot{F}_{SXR} and F_{HXR} . We then examine the relation between $\dot{\mathcal{E}}_e$ and \dot{F}_{SXR} by taking into account the variation of the bremsstrahlung yield.

Correlation of \dot{F}_{SXR} and F_{HXR}

The temporal derivatives of the fluxes of the two *GOES* channels are shown in the bottom panel of Figure 6.1. As is evident, during the rising portion of the *GOES* fluxes the

derivatives of both channels indeed match the first pulse of the *RHESSI* HXR light curves (> 25 keV), but not during the second weaker pulse (where the 1-8 Å derivative shows some instrumental artifacts). This may be due to the fact that the Neupert effect of the second pulse is overwhelmed by the cooling of the hot plasma produced during the first stronger pulse. Nevertheless, the SXR light curves (of both *GOES* and *RHESSI*) exhibit a slightly slower decay rate than that expected from the first pulse alone. This most likely is the signature of the energy input by the second pulse, which slows down the decay of the first pulse.

We note in passing that the SXR light curves start rising several minutes prior to the onset of the HXR impulsive phase. This is an indication of preheating of the plasma before production of a significant number of suprathermal electrons. The 6-12 keV curve rises faster than the *GOES* curves at lower photon energies, which is consistent with the picture that the primary energy release by reconnection occurs high in the corona, where the relatively hotter plasma is heated before significant acceleration of electrons (as suggested in Petrosian & Liu, 2004), and before transport of energy (by accelerated electrons or conduction) down the flare loop to lower atmospheres where cooler plasmas are heated subsequently and produce the *GOES* flux. On the other hand, the increase of the SXR flux at the beginning is dominated by the southern loop, which shows little evidence of chromospheric evaporation. The phenomenon therefore may be a unique feature of this flare.

To quantify the SXR-HXR relationship, we cross-correlated the *RHESSI* 30-50 keV photon energy flux (F_{30-50} ; Fig. 6.12a) and the derivative of the *GOES* low-energy channel flux (\dot{F}_{SXR} ; Fig. 6.12c) in the SXR rising phase (04:58:00-04:59:51 UT). The resulting Spearman rank correlation coefficient (see Fig. 6.12f), an indicator of an either linear or nonlinear correlation, shows a single hump with a maximum value of 0.91 (corresponding to a significance of $\sim 10^{-13}$) at a time lag of 12 s. This suggests a delay of \dot{F}_{SXR} relative to F_{30-50} , which is expected given the finite hydrodynamic response time (on the order of the sound travel time of ~ 20 s for a loop size of $\sim 10^9$ cm and $T \sim 10^7$ K) required for redistribution of the deposited energy. Such a delay is evident in the numerical simulations of Li et al. (1993), who also found that the density enhancement contributes more to the total SXR emissivity than the temperature increase for longer duration (≥ 30 s) HXR bursts during the decay phase. In Figure 6.12d, we plot the two quantities with the *GOES* derivative shifted backward by 12 s to compensate the lag of their correlation. A linear regression (*dotted line*) gives $F_{30-50} = (1.95 \pm 0.15)\dot{F}_{SXR} - (3.68 \pm 0.48)$ with an adjusted coefficient of determination (the so-called *R*-squared) of $R_{adj}^2 = 0.81$, which is close to 1, suggesting a good linear correlation.

Correlation of \dot{F}_{SXR} and $\dot{\mathcal{E}}_e$

We also carried out the same analysis for the electron energy power $\dot{\mathcal{E}}_e$, assuming a thick-target model of power-law electrons with a low-energy cutoff of $E_1 = 25$ keV. We first obtained the energy flux of all the photons with energies greater than E_1 , F_{E_1} , from the 30-50 keV photon energy flux F_{30-50} :

$$F_{E_1} = \int_{E_1}^{\infty} J(E)E dE = F_{30-50} \frac{E_1^{-\gamma+2}}{30^{-\gamma+2} - 50^{-\gamma+2}}, \quad (6.3)$$

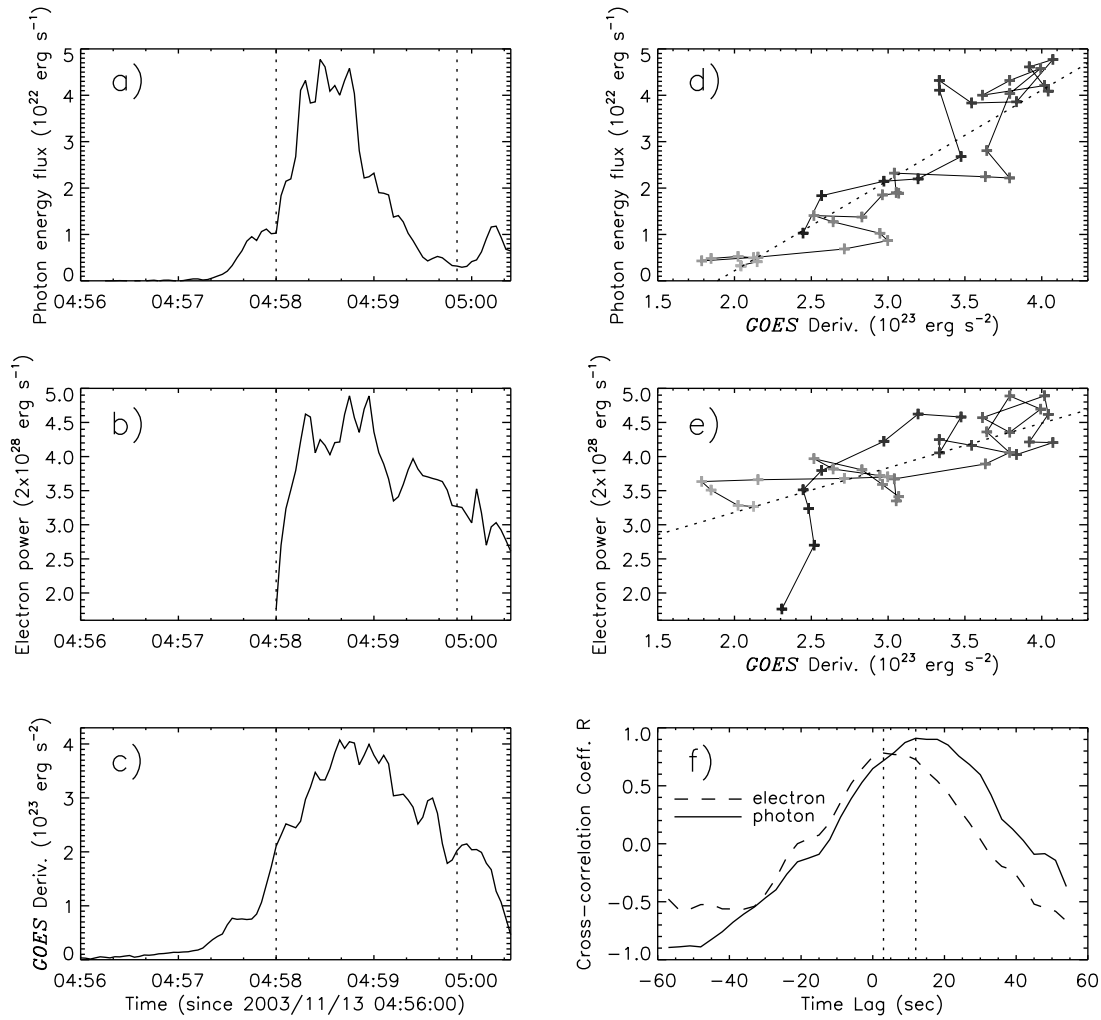


Figure 6.12: (a) Photon energy flux at 30-50 keV (F_{30-50}) at the Sun inferred from the *RHESSI* observation at 1 AU, assuming isotropic emission. The two vertical dotted lines outline the time interval (04:58:00-04:59:51 UT) used for the cross-correlation analysis (see below). (b) Power ($\dot{\mathcal{E}}_e$) of the power-law electrons with a low-energy cutoff of 25 keV inferred from the photon energy flux assuming a thick-target model. (c) Same as (a) but for the derivative (\dot{F}_{SXR}) of the *GOES* low-energy channel (1-8 Å) flux. (d) HXR energy flux F_{30-50} vs. SXR derivative \dot{F}_{SXR} (shifted back in time by 12 s to account for its delay, as revealed by the cross-correlation analysis; see f) within the interval of 04:58:00-04:59:51 UT. The gray scale of the plus signs (connected by the solid lines) from dark to light indicates the time sequence. The dotted line is the best linear fit to the data. (e) Same as (d) but for $\dot{\mathcal{E}}_e$ and \dot{F}_{SXR} , which is shifted back by 3 s in time. (f) Spearman rank correlation coefficient R of the photon energy flux (electron power) and \dot{F}_{SXR} plotted as a function of time lag of the latter relative to the former. The dotted lines mark the peak values of $R = 0.91$ and 0.78 at a lag of 12 and 3 s, respectively [from Liu, W. et al. 2006].

where $J(E) \propto E^{-\gamma}$ is the photon flux distribution at the Sun (in units of photons $\text{keV}^{-1} \text{s}^{-1}$), which is obtained from spectrum fitting (see §6.2.2) and is assumed to extend to infinity in energy space. We then calculated the power of the electrons by

$$\dot{\mathcal{E}}_e = F_{E_1}/Y_{E_1}, \quad (6.4)$$

where the bremsstrahlung yield Y_{E_1} is given by equation (6.2).¹⁰ The resulting value of $\dot{\mathcal{E}}_e$ is plotted versus time and versus the *GOES* derivative in Figures 6.12*b* and 6.12*e*, respectively. The dotted line in Figure 6.12*e* shows a linear fit ($R_{adj}^2 = 0.49$) to the data: $\dot{\mathcal{E}}_e = (0.65 \pm 0.11)\dot{F}_{SXR} + (1.88 \pm 0.34)$. The corresponding Spearman rank correlation coefficient has a peak value of 0.78 (significance of $\sim 10^{-8}$) at a time lag of 3 s (Fig. 6.12*f*). As evident, $\dot{\mathcal{E}}_e$ yields no better correlation with \dot{F}_{SXR} than F_{30-50} does, which is similar to the conclusion reached by Veronig et al. (2005). During the HXR decay phase (after 04:59:20 UT), the spectrum becomes softer ($\gamma > 5$) and $\dot{\mathcal{E}}_e$ decreases much slower than F_{30-50} , since the bremsstrahlung yield (eq. [6.2]) decreases with the spectral index. As noted above, for these high spectral indexes, the emission might be thermal rather than nonthermal. The inferred electron power is thus highly uncertain for these times.

As stated earlier, the total energy of the nonthermal electrons is very sensitive to the low-energy cutoff E_1 , which is generally not well determined (cf. Sui et al., 2005). We thus set E_1 as a free parameter and repeat the above calculation for different values of E_1 (ranging from 15 to 28 keV). We find that, as expected, the temporal $\dot{\mathcal{E}}_e$ - \dot{F}_{SXR} relationship highly depends on the value of E_1 . For a small value of E_1 ($\lesssim 20$ keV), $\dot{\mathcal{E}}_e$ keeps rising until $\sim 04:59:50$ UT (near the bottom of the F_{30-50} light curve), which makes the $\dot{\mathcal{E}}_e$ - \dot{F}_{SXR} correlation completely disappear. On the other hand, for a large value of E_1 (> 20 keV), the correlation is generally good during the impulsive pulse (through 04:59:10 UT), and the larger the value of E_1 , the better the correlation. This is because the conversion factor $E_1^{-\gamma+2}/(30^{-\gamma+2} - 50^{-\gamma+2})$ in equation (6.3) is an increasing (decreasing) function of the photon spectral index γ if value of E_1 is sufficiently small (large). For a small value of E_1 , for example, the photon energy flux F_{E_1} may have a somewhat large value in the valley of the F_{30-50} light curve when γ is high. In addition, during this time interval the bremsstrahlung yield Y_{E_1} becomes small, since δ is large (see eq. [6.2]), and consequently this may result in a very large value of $\dot{\mathcal{E}}_e$ by equation (6.4).

As to the magnitude of the energy flux of nonthermal electrons, Fisher et al. (1985c) in their HD simulations found that the dynamics of the flare loop plasma is very sensitive to its value. For a low-energy flux ($\leq 10^{10}$ ergs $\text{cm}^{-2} \text{s}^{-1}$), the upflow velocity of the evaporating plasma is approximately tens of km s^{-1} ; for a high-energy flux ($\geq 3 \times 10^{10}$ ergs $\text{cm}^{-2} \text{s}^{-1}$), a maximum upflow velocity of approximately hundreds of km s^{-1} can be produced. For the flare under study, we estimate the area of the cross-section of the loop to be $A_{loop} \lesssim 1.6 \times 10^{18} \text{ cm}^2$, where the upper limit corresponds to the loop width determined by the 5% level in Figure 6.4*b*. We read the maximum electron power of $\dot{\mathcal{E}}_{e,max} = 9.8 \times 10^{28}$ ergs s^{-1} from Figure 6.12*b*, which is then divided by $2A_{loop}$ (assuming a filling factor of unity) to yield the corresponding electron energy flux: $f_{e,max} \gtrsim 3.1 \times 10^{10}$ ergs $\text{cm}^{-2} \text{s}^{-1}$.

¹⁰We used more accurate results from numerical integration of eq. (29) in Petrosian (1973), rather than the approximate eq. (6.2) here. However, one can still use eq. (6.2) with a simple correction factor of $0.0728(\delta - 4) + 1$ in the range $4 \leq \delta \leq 9$ to achieve an accuracy of $\lesssim 1\%$.

The source velocity estimated in §6.2.1 on the order of a few hundred km s^{-1} is consistent with that predicted by Fisher et al. (1985c). For comparison, we note that Milligan et al. (2006) also obtained an energy flux of $\geq 4 \times 10^{10} \text{ ergs cm}^{-2} \text{ s}^{-1}$ from *RHESSI* data for an M2.2 flare during which an upflow velocity of $\sim 230 \text{ km s}^{-1}$ was inferred from simultaneous co-spatial *SOHO* Coronal Diagnostic Spectrometer (CDS) Doppler observations.

In summary, the *GOES* SXR flux derivative \dot{F}_{SXR} exhibits a Neupert-type linear correlation with the *RHESSI* HXR flux F_{30-50} during the first HXR pulse. However, unexpectedly, the correlation between the electron power $\dot{\mathcal{E}}_e$ and \dot{F}_{SXR} is not well established on the basis of the simple analysis presented here, which suggests that a full HD treatment is needed to investigate the chromospheric evaporation phenomenon (see discussions in §6.4).

6.3 Loop Density Derivation

For the 1994 June 20 disk flare, Silva et al. (1997) interpreted the moving SXR sources as thermal emission from the hot ($\sim 30 - 50 \text{ MK}$) plasma evaporated from the chromosphere on the basis of the good agreement of the emission measure of the blueshifted component and that of the SXR from the FPs. For the limb flare under study here, Doppler shift measurements are not available. Meanwhile, a purely thermal scenario would have difficulties in explaining the systematic shift of the centroids towards the FPs with increasing energies up to $\sim 70 \text{ keV}$, as shown in Figure 6.9. A nonthermal scenario appears more appropriate. That is, the apparent HXR FP structure and motions can result from a decrease in the stopping distance of the nonthermal electrons with decreasing energy and/or increasing ambient plasma density caused by the chromospheric evaporation (as noted earlier in §6.2.1). One can therefore derive the density distribution along the loop from the corresponding X-ray emission distributions (e.g., Fig. 6.7) without any preassumed density model (cf. Aschwanden et al., 2002). This approach is described as follows.

For a power-law X-ray spectrum produced by an injected power-law electron spectrum, Leach (1984) obtained a simple empirical relation (also see Petrosian & Donaghy, 1999, §2) for the X-ray intensity $I(\tau, k)$ per unit photon energy k (in units of 511 keV) and column depth τ [in units of $1/[4\pi r_0^2 \ln \Lambda] = 5 \times 10^{22} \text{ cm}^{-2}$ for $r_0 = 2.8 \times 10^{-13} \text{ cm}$ and $\ln \Lambda = 20$]:

$$I(\tau, k) = A \left(\frac{\delta}{2} - 1 \right) \left(\frac{k+1}{k^{2+\gamma}} \right) \left(1 + \tau \frac{k+1}{k^2} \right)^{-\delta/2}, \quad (6.5)$$

where γ and δ (which is equal to $\gamma + 0.7$) are the photon and electron spectral indexes, respectively, A is a constant normalization factor, and $d\tau = nds$, where s is the distance measured from the injection site. This equation quantifies the dependence of the emission profile (or source morphology) on the electron spectral index and column depth. In general, when δ decreases (spectrum hardening), the intensity at a given photon energy rises (drops) at large (small) values of τ and thus the emission centroid shifts to larger values of τ . This is expected because for a harder spectrum, there are relatively more high-energy electrons that can penetrate to larger column depths and produce relatively more bremsstrahlung photons there. The opposite will happen when the spectrum becomes softer. During the impulsive peak, which shows a soft-hard-soft behavior (see §6.2.2), one would expect that the emission centroids would shift first away from and then back toward the LT (if the

density in the loop stays constant). If we know the spectral index, the emission profile can therefore yield critical information about the density variation in both space and time.

To compare the above empirical relation with observations, we first integrate $I(\tau, k)$ over an energy range $[k_1, k_2]$,

$$J(\tau; k_1, k_2) = \int_{k_1}^{k_2} A \left(\frac{\delta}{2} - 1 \right) \left(\frac{k+1}{k^{2+\gamma}} \right) \left(1 + \tau \frac{k+1}{k^2} \right)^{-\delta/2} dk, \quad (6.6)$$

and then integrate $J(\tau; k_1, k_2)$ over τ to obtain the cumulative emission,

$$F(\tau; k_1, k_2) = \int_0^\tau J(\tau; k_1, k_2) d\tau = \frac{1-\gamma}{k_2^{1-\gamma} - k_1^{1-\gamma}} \int_{k_1}^{k_2} \left[1 - \left(1 + \tau \frac{k+1}{k^2} \right)^{1-\delta/2} \right] k^{-\gamma} dk, \quad (6.7)$$

where we have chosen

$$A = \left(\int_{k_1}^{k_2} k^{-\gamma} dk \right)^{-1} = \frac{1-\gamma}{k_2^{1-\gamma} - k_1^{1-\gamma}}, \quad (6.8)$$

so that $F(\tau = \infty; k_1, k_2) = 1$. Comparison of $F(\tau; k_1, k_2)$ with the observed emission profiles gives the column depth $\tau(s)$, whose derivative with respect to s then gives the density profile along the loop.

Specifically for this flare, we assume that the nonthermal electrons are injected at the LT indicated by the middle vertical dotted line in Figure 6.7 and denote the profile to the right-hand side of this line (i.e., along the northern half of the loop) as $J_{obs}(s; k_1, k_2)$, where $[k_1, k_2]$ is the energy band of the profile. The observed cumulative emission is then given by

$$F_{obs}(s; k_1, k_2) = \frac{\int_0^s J_{obs}(s; k_1, k_2) ds}{\int_0^{s_{max}} J_{obs}(s; k_1, k_2) ds}, \quad (6.9)$$

where s_{max} (corresponding to $\tau = \infty$) is the maximum distance considered and $F_{obs}(s; k_1, k_2)$ has been properly normalized. Then $\tau = \tau(s; k_1, k_2)$ can be obtained by inverting

$$F(\tau; k_1, k_2) = F_{obs}(s; k_1, k_2), \quad (6.10)$$

where the integration over k in equation (6.7) can be calculated numerically.

It should be noted, however, that not all the profiles in Figure 6.7 are suitable for this calculation, because low-energy emission is dominated by a thermal component, especially in the LT region and at later times. We thus restrict ourselves to the energy ranges of 12-72, 13-72, and 17-72 keV, respectively, for the three 24 s intervals. The lower bound is the energy above which the power-law component dominates over the thermal component, determined from fits to the spatially integrated spectrum for each interval, as shown in Figure 6.13. Within these energy ranges, separate leg or FP sources rather than a single LT source can be identified in the corresponding image, which is morphologically consistent with the nonthermal nature of emission assumed here. To further minimize the contamination of the thermal emission in our analysis, we have excluded the LT portion of the emission profile in excess of the lowest local minimum (if it exists) between the LT and leg (or FP) sources. An example of this exclusion is illustrated by the hatched region in Figure 6.7c for

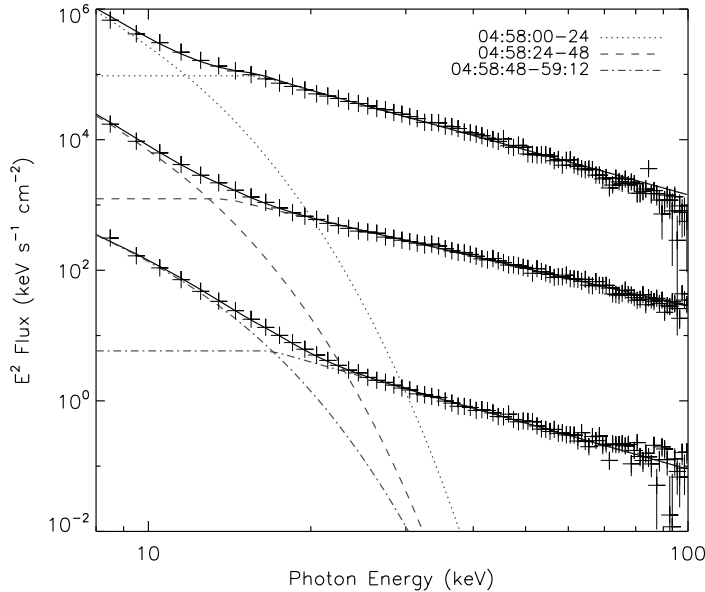


Figure 6.13: Spatially integrated spectra (νF_ν) for the three 24 s time intervals, as indicated in the legend. From the top to the bottom, the second and third spectra are shifted downward by 2 and 4 decades, respectively. The broken lines indicate the thermal and power-law components of the fits to the data, and the solid lines are the sum of the two components. The thermal and power-law components intersect at about 12, 13, and 17 keV, respectively for the three intervals, above which the power-law component dominates [from Liu, W. et al. 2006].

the 19-21 keV profile. This was done by simply replacing the profile values between the LT and the local minimum positions with the value at the minimum.

We calculated $\tau(s; k_1, k_2)$ for every emission profile within the energy ranges mentioned above for the three intervals in Figure 6.7, with photon indexes of $\gamma = 4.46, 3.97,$ and $4.23,$ respectively. From the geometric mean of the column depths obtained at different energies, $\bar{\tau}$, we derived the density profile $n(s) = d\bar{\tau}(s)/ds$ for each time interval. The results are shown in Figure 6.14, where we bear in mind that attention should be paid to the overall trend rather than the details of the density profile and its variation, because the profile here only spans about 3 times the resolution ($\sim 7''$) and thus is smoothed, making neighboring points not independent. As can be seen, between the first and second intervals, the density increases dramatically in the lower part of the loop, while the density near the LT remains essentially unchanged. The density enhancement then shifts to the LT from the second to the third interval. This indicates a mass flow from the chromosphere to the LT. The density in the whole loop is about doubled over the three intervals, which is roughly consistent with the density change inferred from the emission measure¹¹ (see Fig. 6.10*d*). These results are again compatible with the chromospheric evaporation picture discussed in §6.2.1.

¹¹From 04:58:12 through 04:59:00 UT, the *RHESSI* (*GOES*) emission measure rises by a factor of 5.3 (2.3), which translates to an increase of the density by a factor of 2.3 (1.5), assuming a constant volume.

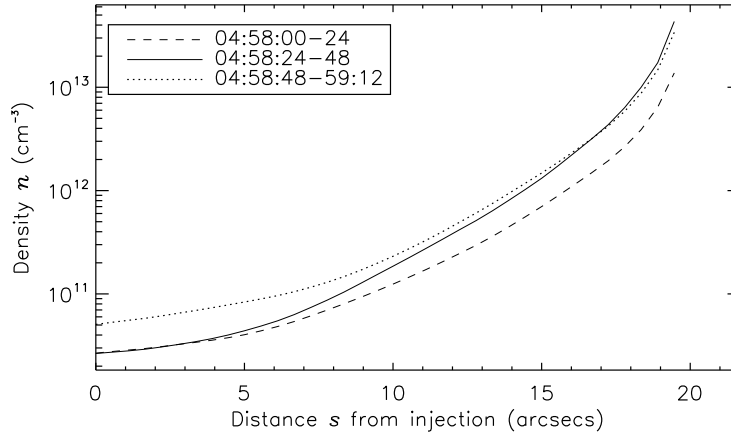


Figure 6.14: Averaged density profiles along the loop inferred from the HXR brightness profiles during the three time intervals [from Liu, W. et al. 2006].

6.4 Summary and Discussion

We have presented in this chapter a study of *RHESSI* images and spectra of the 2003 November 13 M1.7 flare. *RHESSI*'s superior capabilities reveal great details of the HXR source morphology at different energies and its evolution during the impulsive phase. The main findings are as follows.

1. The energy-dependent source morphology in general shows a gradual shift of emission from the LT to the FPs with increasing energies. Over some short integration intervals, emission from the loop legs may dominate at intermediate energies.
2. The emission centroids move toward the LT along the loop during the rising and plateau portions of the impulsive phase. This motion starts at low energies and proceeds to high energies. We estimate the mean velocity of the motion to be hundreds of km s^{-1} , which agrees with the prediction of the hydrodynamic simulations by Fisher et al. (1985c). There are also shorter time scale variations that imply much higher velocities ($\sim 10^3 \text{ km s}^{-1}$) but we are not certain if they are real because of instrumental limitations.
3. Fits to the spatially integrated *RHESSI* spectra with a thermal plus power-law model reveal a continuous increase of the emission measure (EM) while the temperature does not change significantly. The *GOES* data show a similar trend of the EM but a gradual increase of the temperature.
4. The time derivative of the *GOES* SXR flux is correlated with the *RHESSI* HXR flux, with a peak correlation coefficient of 0.91 at a delay of 12 s, in agreement with the general trend expected from the Neupert effect. However, the correlation between the electron power and the *GOES* derivative is no better than the SXR-HXR correlation.

5. From the observed brightness profiles, we derive the spatial and temporal variation of the plasma density in the loop, assuming a nonthermal thick-target bremsstrahlung model. We find a continuous increase of the density, starting at the FPs and legs and then reaching to the LT. All these results fit into a picture of continuous chromospheric evaporation caused by the deposition of energy of electrons accelerated during the impulsive phase.

Several of the new features of this event (such as the leg emission at intermediate energies) may be common to many solar flares. Expanding the sample of flares of this kind will be very helpful in understanding the underlying physical processes. The new findings reside near the limit of *RHESSI*'s current temporal, spatial, and spectral resolution. As advanced imaging spectroscopy capabilities are being developed and spatial resolution is being improved in the *RHESSI* software (Hurford et al., 2002), it will be critical to obtain the spatially resolved photon spectrum along the loop. This will yield incisive clues to the nature of the moving X-ray sources and relevant energy transport mechanisms and will be useful to check the reality of the short-timescale variations.

There are several important questions that need to be further addressed in future observational and theoretical investigations: (1) What is the nature of the moving X-ray sources? Could they be characterized as thermal emission from the evaporated hot plasma or as nonthermal emission from the precipitating electrons, or a mixture of both? Could they be related to magnetohydrodynamic (MHD) waves or evaporation fronts? (2) What are the roles of different heating agents of the chromosphere; that is, electron beams, thermal conduction, and/or direct heating by turbulence or plasma waves during the impulsive phase?

We have pointed out some of the many physical processes that come into play in answering such questions. Here we describe possible directions for future theoretical studies. We have shown that a more physical test of the Neupert effect between the electron power and the SXR flux derivative does not reveal a better correlation than the usual HXR versus SXR derivative correlation. Although the observed source velocity agrees with those of HD simulations, there are some features that current simulations have not addressed. To answer these questions requires an updated numerical calculation in which one combines the model of particle acceleration and transport with the HD simulation of the atmospheric response to energy deposition to form a unified picture of solar flares. For example, one can use the output electron spectrum from the stochastic particle acceleration model (Hamilton & Petrosian, 1992; Miller et al., 1997; Park et al., 1997; Petrosian & Liu, 2004) as the input to the transport and HD codes rather than simply assuming a power-law electron spectrum, as in previous HD simulations. Such a study can shed light on the relative importance of particle beams and thermal conduction in evaporating chromospheric plasma and the roles that MHD waves may play in heating the flaring plasma; in particular, addressing our tentative observation of the fast source motion, which suggests possible presence of MHD waves in the flare loop. A better understanding of their propagation, damping, and excitation mechanisms is necessary for uncovering the energy release process during flares. In the following two chapters, we will present our combined Fokker-Planck and HD simulations along this line of research.